Investigations on electronic structure of $YMnO_3$ by electron energy loss spectra and first-principle calculations

S. Wang,[1] J. Cai,[2] H. D. Xu,[1] H. L. Tao,[1] Y. Cui,[1] Z. H. Zhang,[1] B. Song,[3] S. M. Liu,[1] and M. He [1,a)]
[1]*School of Materials Science and Engineering, Dalian Jiaotong University, Dalian 116028, China*
[2]*School of Physics and Electronic Technology, Liaoning Normal University, Dalian 116029, China*
[3]*Academy of Fundamental and Interdisciplinary Sciences, Harbin Institute of Technology, Harbin 150080, China*

(Received 15 May 2019; accepted 15 July 2019)

Crystal structure and electronic structure of $YMnO_3$ were investigated by X-ray diffraction and transmission electron microscopy related techniques. According to the density of states (DOS), the individual interband transitions to energy loss peaks in the low energy loss spectrum were assigned. The hybridization of O 2p with Mn 3d and Y 4d analyzed by the partial DOS was critical to the ferroelectric nature of $YMnO_3$. From the simulation of the energy loss near-edge structure, the fine structure of O K-edge was in good agreement with the experimental spectrum. The valence state of Mn (+3) in $YMnO_3$ was determined by a comparison between experiment and calculations.
 [doi:10.1017/S0885715619000617]

Key words: electronic structure, X-ray diffraction, electron energy-loss spectroscopy, first-principle calculation

I. INTRODUCTION

Ferroelectric materials have attracted great interest in fundamental research owing to their potential technological applications (Du *et al.*, 2008; Gibbs *et al.*, 2011; Malo and Maignan, 2012). $YMnO_3$ exhibits multiferroicity with high ferroelectric and low antiferromagnetic transition temperature (Huang *et al.*, 1997; Lin *et al.*, 2019a, 2019b). It belongs to the non-center symmetric space group of $P6_3cm$ at room temperature with typical ABO_3-type structure (Prikockyte *et al.*, 2011; Bi *et al.*, 2019; He *et al.*, 2019). A prototype ferroelectricity was observed in the so-called d^0-ness systems, such as $BaTiO_3$, in which $Ti^{4+}(d^0)$ ions make off-center movements in TiO_6 octahedra to lower the energy through enhanced Ti 3d and O 2p hybridization (Cohen, 1992; Ghosez *et al.*, 1998; Babu *et al.*, 2007). $YMnO_3$ contains Mn ($3d^4$) magnetic ions. Thus, a mechanism other than "d^0-ness" is needed to account for the ferroelectricity. Possibilities include lone pair electrons as in $BiMnO_3$ or a spin frustration of magnetic order as in $TbMnO_3$ (Kimura *et al.*, 2003). But neither lone pair nor spin frustration can explain the ferroelectricity of $YMnO_3$.

The ferroelectricity mechanism for $YMnO_3$ has been ambiguous and confusing so far. Filippetti and Hill performed density functional theory (DFT) calculations and proposed that distortion was caused by hybridization between unoccupied Mn $3d_z^2$ and O $2p_z$ orbitals (Filippetti and Hill, 2002). Cho performed the polarization-dependent X-ray absorption spectroscopy and concluded that Y 4d states were strongly hybridized with the O 2p states (Cho *et al.*, 2007). Liu proposed that the ferroelectric origin of $YMnO_3$ was associated with the charge transfer from the Y–O bonds to the Mn–O bonds (Liu *et al.*, 2011), etc. However, these works did not systematically combine experiments with calculations when discussing the electronic structure of $YMnO_3$.

X-ray diffraction (XRD) and electron energy loss spectroscopy (EELS) are two important methods for characterization of materials and condensed matter. Combining with the XRD results, EELS can provide additional information. When incident electrons enter a material, they interact with the constituent atoms via electrostatic forces. As a result of these forces, some of the electrons are scattered. The interaction between incident electrons and the atomic electrons surrounding the nucleus is inelastic scattering. By analyzing the energy loss distribution of inelastic scattered electrons, the spatial environment information of the electrons can be obtained, and various physical and chemical properties of the sample can be studied. (Egerton *et al.*, 1987; Zhang *et al.*, 2008; Lin *et al.*, 2019a, 2019b; Wang *et al.*, 2019a, 2019b). First-principle calculations were used to analyze the single-electron excitation from the valence band (VB) to the conduction band (CB) in EELS experiments. The empty density of states (DOS) can be comparable with the energy loss near-edge structure (ELNES) (Ikeno and Mizoguchi, 2017; Wang *et al.*, 2018). In this work, we combined the first-principle calculations with EELS experiments, valence EELS were obtained and analyzed by the calculated DOS, ELNES were investigated by comparing the simulated results with experiments to study the electronic structure of $YMnO_3$. The results provided a theoretical basis for understanding the ferroelectric mechanism of $YMnO_3$.

II. EXPERIMENTAL METHODS AND THEORETICAL DETAILS

The $YMnO_3$ sample was prepared using a conventional solid-state reaction method (Zhang *et al.*, 2014). The XRD measurements were performed in the EMPYREAN X-ray diffractometer from Dutch PANalytical company (with the

a)Author to whom correspondence should be addressed. Electronic mail: heming@djtu.edu.cn

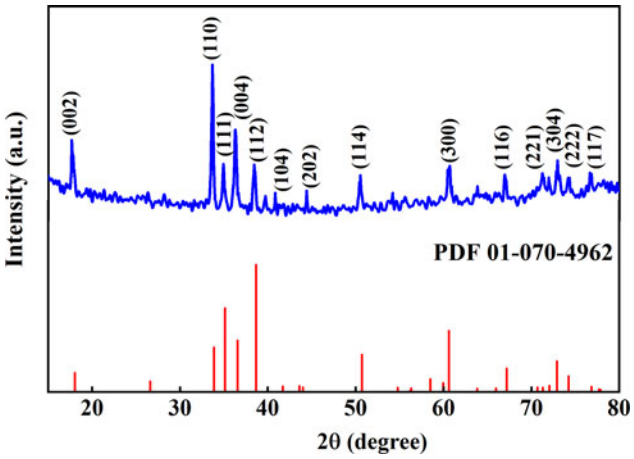

Figure 1. XRD pattern of the collected powders, the position of diffraction peaks is almost the same with the standard card (PDF 01-070-4962).

detector PIXcel-3D). The powder sample was flattened onto the glass piece and loaded into the fixture. The measurements were carried out in the Bragg Brentano $\theta-2\theta$ geometry with Cu$K\alpha$ radiation at an operating voltage of 40 kV and an operating current of 40 mA. The samples were scanned from 10° to 130° with the step size of 0.26261°, and the dwell time is 39.53 s step^{-1}. HighScore software was used to smooth the data, eliminate the alpha-2, and refine the lattice parameter. The EELS experiments were performed using a post-column Gatan Imaging Filter system attached to the microscope with an energy resolution of 1.0 eV for core-loss EELS. Its energy resolution was determined by the full-width half-maximum of the zero-loss peak. The spectra were acquired in selected area electron diffraction (SAED) mode at small momentum transfer. The energy dispersion is 0.2 eV pixel^{-1}. All of the spectra were calibrated using the zero-loss peak position.

The calculations were performed using the DFT in Cambridge Serial Total Energy Package (CASTEP). Ultrasoft pseudopotential was expanded within a plane wave basis set to ensure the convergence with the cut-off energy (450 eV). Integrations in Brillouin zone were performed using special k-points generated with $4 \times 4 \times 2$ mesh parameters grid. Exchange and correlation effects were described by Perdew–Burke–Ernzerhof (PBE) in generalized gradient approximation (Perdew *et al.*, 1996). During the optimization, the convergence criteria of the energy and the maximum force were set at 1.0×10^{-5} eV atom^{-1} and 0.05 eV Å^{-1}. The maximum stress was less than 0.1 GPa and the displacement of atoms convergence should be less than 0.002 Å.

III. RESULTS AND DISCUSSIONS

Figure 1 presents XRD patterns of the $YMnO_3$ powders. Compared with the standard card (PDF 01-070-4962), the position of the diffraction peaks is almost the same, so it is shown that the powder sample is in $P6_3cm$ hexagonal structure. Therefore, the $YMnO_3$ of ferroelectric phase was determined by XRD experiments, which provided a qualitative basis for EELS experiments. And the standard card provides atomic structure information for the simulated calculation ($a = 6.1390$ Å, $b = 6.1390$ Å, $c = 11.4070$ Å, $\alpha = 90°$, $\beta = 90°$, $\gamma = 120°$). Figure 2 presents the crystal structure of the optimized hexagonal $YMnO_3$, the primitive unit cell contains six formula units (30 atoms). Two inequivalent Y_1 (0, 0, 0.771) and Y_2 (0.334, 0.667, 0.730) atoms form layers between the MnO_5 triangular bipyramids tilted with respect to c-axis.

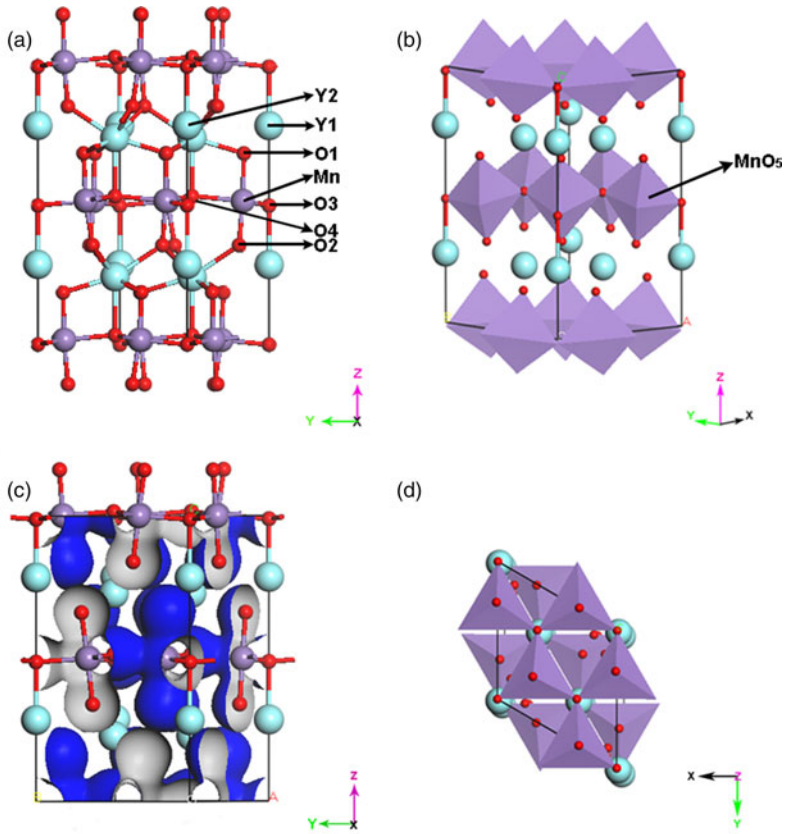

Figure 2. (a) Atomic structure of the $P6_3cm$ ferroelectric $YMnO_3$. (b) The triangular bipyramids of MnO_5 in the atomic model. (c) Three-dimensional electron density distribution of $YMnO_3$ obtained by CASTEP calculation. (d) Atomic structure with z-axis perpendicular to the paper surface.

https://doi.org/10.1017/S0885715619000617 Published online by Cambridge University Press

TABLE I. Calculated equilibrium lattice constants and selected interatomic distances (Å) in $YMnO_3$ crystal compared to experimental data.

	Cal. (Salazar-Kuri *et al.*, 2012)	Exper. (Lima and Lalic, 2013)
a	6.139	6.155
c	11.407	11.403
Mn–O1	1.863	1.850
Mn–O2	1.862	1.878
Mn–O3	2.073	1.996
Mn–O4	2.052	2.097
Y1–O1	2.281	2.345
Y2–O1	2.275	2.459
Y1–O2	2.316	2.282
Y2–O2	2.300	2.283
Y1–O3	2.326	2.345
Y2–O4	2.452	2.459

Equivalent Mn atoms (0.335, 0.335, 0.497) are situated in the center of MnO_5, which is surrounded by O3 (0, 0, 0.475), $O4_1$ (0.334, 0.667, 0.516), $O4_2$ (0.667, 0.334, 0.516) in the plane (O_P) perpendicular to the *c*-axis, O1 (0.359, 0.359, 0.334) and O2 (0.308, 0.308, 0.660) along the *c*-axis (O_T). The lattice constant and interatomic distance were obtained from the literature by Salazar-Kuri *et al.* (2012), and we used these data to build the atomic structure of $YMnO_3$. The related parameters and corresponding experimental values (Lima and Lalic, 2013) are presented in Table I. As it can be seen, the calculated parameters are consistent with the experimental data. The electron density distribution around the Mn ion in Figure 2(c) is anisotropic. The minimum electron densities of the Mn–O_T bonds are larger than that of the Mn–O_P bonds. The results can be described to the conventional localized bonding electrons, because the Mn–O_T bonds (~1.9 Å) are quite shorter than the Mn–O_P bonds (2.1 Å). Figure 3(a) is the SAED diagram under [1$\bar{1}$0] zone axis. Figure 3(b) shows the high-resolution transmission electron microscopy (HRTEM) results. The measured interplanar spacings were about 0.281 and 0.305 nm, which are comparable with the planes of (004) and (110) in the XRD, respectively. The matching planes shown by SAED are also (004) and (110). Moreover, the SAED pattern in Figure 2(a) is consistent with the FFT pattern [inset of Figure 2(b)] of the HRTEM image.

The single-scattering distribution $S(E)$ of $YMnO_3$ is shown in Figure 4(a), which is extracted by the removal of the plural scattering using Fourier-log deconvolution (Egerton, 2009). One important step to gain $S(E)$ is the removal of the zero-loss peak, as emphasized by our previous work (Zhang *et al.*, 2006), because it is high-energy tail covers features of the low-loss region (Rafferty *et al.*, 2000; Erni and Browning, 2005). Above the bandgap, there are five well-resolved peaks, located at ~6.40 eV (A_1), ~10.21 eV (A_2), ~14.07 eV (A_3), ~21.39 eV (A_4) and ~34.49 eV (A_5), respectively. The dominant peak A_5 can be assigned to the bulk-plasmon oscillation. Other peaks originate from the single electron excitation from the VB to the empty DOS in the CB, and their profiles are expected to have a direct correlation with the joint DOS between occupied and unoccupied states in the energy bands. It should be noted, most of the peaks have mixed character since the dipole transitions selection rules have been extended. In the case of a large collection aperture, dipole-forbidden transitions ($\Delta L = 2$) are sometimes observed (Egerton *et al.*, 1987; Lin *et al.*, 2017; Quhe *et al.*, 2019). Thus, A_1 is mainly attributed to the transitions between the O 2p to the Mn 3d band. A_2 agrees with the characteristic of the O 2p to the Mn 3d/Y 4d transitions; meanwhile, the Mn 3d to the Y 4d transitions also make contributions to it. A_3 corresponds to the excitation from the O 2p or Mn 3d to the Y 4d level. A_4 corresponds to the transitions from the O 2s to the Mn 3d. For convenience, the assignments of the corresponding transitions were added to Table II. We found that every energy loss peak is related to the electronic transitions from the O 2p orbital to the Mn 3d or Y 4d orbitals. The information about electronic structure can be obtained from Figure 4(b). In the VB, the primarily populated O 2p and Mn 3d states form a block of the states whose energy lies approximately between −6.7 and −1.1 eV, within this energy range Mn atoms and O atoms exhibits hybridization. The energy range of −18.8 to −17.3 eV is mainly filled by a relatively narrow band of the 2s orbital electrons of O atoms. In the VB, only a small amount of Y 4d states are concentrated in the energy range from −6.6 to −1.7 eV, while the Y 4d states are mainly concentrated in the CB between 5.6 and 7.4 eV. The energy level from 2.8 to 7.1 eV is mainly occupied by the 3d orbital electrons of Mn atoms and is filled by little O 2p states.

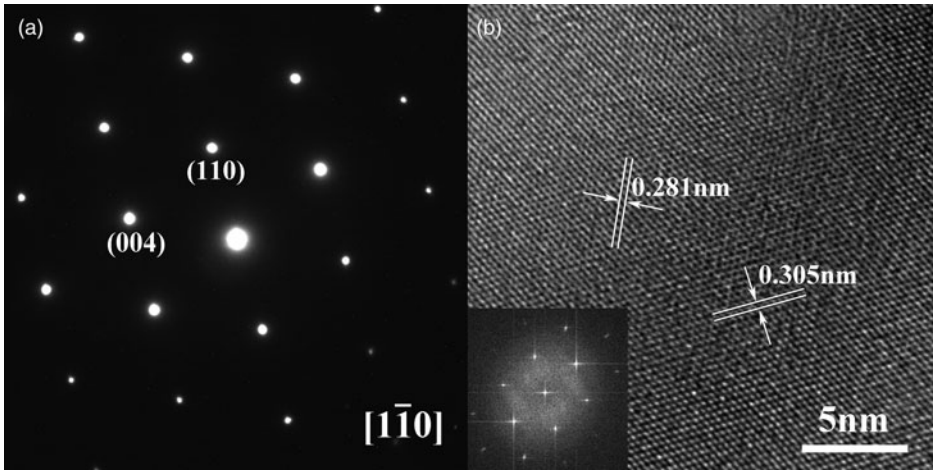

Figure 3. (a) SAED pattern recorded from [1$\bar{1}$0] zone axis. (b) HRTEM image shows three different lattice directions, the left bottom shows the pattern after Fast Fourier Transform (FFT).

https://doi.org/10.1017/S0885715619000617 Published online by Cambridge University Press

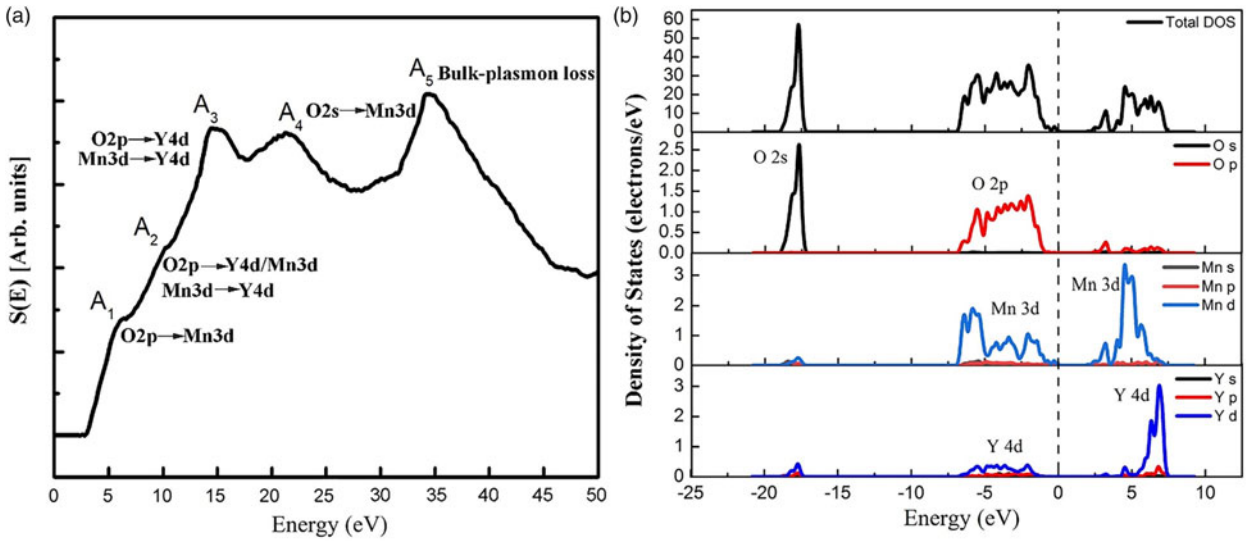

Figure 4. (a) The low energy loss spectrum of $YMnO_3$. The intensity maximum around 34.49 eV is assigned to the bulk-plasmon loss, the smaller features are due to excitation from interband transitions. (b) Total and partial DOS in $YMnO_3$. The fermi level is set at 0 eV.

TABLE II. Assignment of the major interband transition between experiment and theory.

Transition	Energy (eV)	Predominant orbital character
A_1	6.40	O2p–Mn3d
A_2	10.21	O2p–Y4d/Mn3d, Mn3d–Y4d
A_3	14.07	O2p/Mn3d–Y4d
A_4	21.39	O2s–Mn3d
A_5	34.49	Bulk-plasmon loss

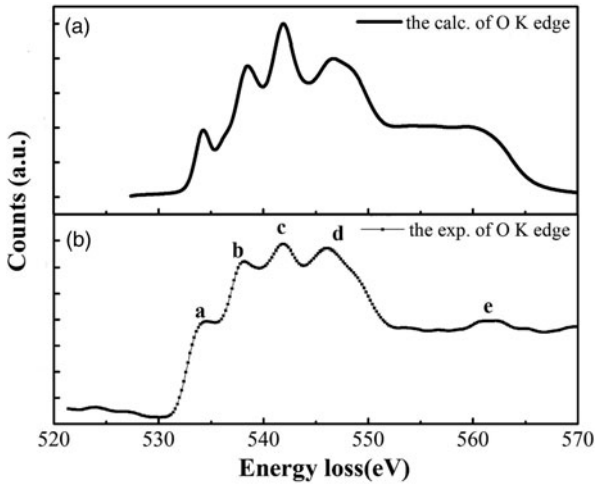

Figure 5. (a) The simulation spectrum of O K-edge with core-hole effects. (b) The experimental spectrum of O K-edge.

Overall, the local symmetry of the Mn is bipyramidal, thus the energy of its 3d orbital splits into doublets: in the VB top consists of the mixture of the e_{1g} and a_{1g} states, while the CB bottom is formed of the mixture of the a_{1g}, e_{1g} and t_{1g} states (Sotero *et al.*, 2015). We also observed from the figure that the 4d orbital electrons of Y atoms and the 2p orbital electrons of O atoms have hybrid processes in both VB and CB, but the hybridization intensity is not stronger than Mn3d and O2p. Thus, the analysis of the DOS showed that the interaction among 2p of O, 3d of Mn, and 4d of Y atomic orbitals causes the spontaneous polarization, which results in the appearance of ferroelectric phase.

To get more information about the electronic structure, we have carried out ELNES studies. The ELNES reflect both compositional analysis and degree of bonding hybridization. Thus, it contains valuable information about the nearest neighbored bonding (O 2p with the cationic *d*-orbital). Figure 5 shows the results of O K-edge by calculation and experiment. We can see that the simulated spectra nearly reproduce all details presented in the fine structure in terms of number of peaks, peak intensity and peak position. The O K-edge fine structure reflects mainly the density of O 2p states when hybridized with Y and Mn orbitals from the $YMnO_3$. In Figure 5(b), five characteristic peaks marked by *a*, *b*, *c*, *d* and *e* can be clearly distinguished, where peaks a and b are related to the hybridization between O and Mn ions, and peaks c and d reflect the hybridization between O and Y ions. It indicates that O–Mn and O–Y covalent bonds are formed between O atoms and Mn/Y atoms, which has a stabilizing effect on the ferroelectric phase. The feature group of *e* is an absorption peak, which is a diffractive region due to a backscattering process between the absorber and its nearest neighbor oxygen shell (Kim *et al.*, 2014; Wang *et al.*, 2019a, 2019b). In Figure 6, there are two main peaks of Mn $L_{2,3}$ edge in the experiment and calculations, which are originating from the electron transition from $2p_{3/2}$ and $2p_{1/2}$ states to unoccupied 3d bands (Nishida *et al.*, 2013). The L_3/L_2 ratio is known to be related to the valence state of the 3d transition metal. And the ratio of Mn L_3/L_2 in this work was estimated using the method reported by Varela *et al.* (2009). The integrated areas of the Mn $L_{2,3}$ edge used to estimate L_3/L_2 ratio are shown in Figure 6(c), and the ratio is about 2.46. It can be confirmed from related literature that the Mn of the $YMnO_3$ compound is between trivalent and tetravalent oxidation states (Schmid and Mader, 2006). We simulated two valence states of Mn shown in Figures 6(a) and 6(b), and the simulated spectrum with Mn (+3) is in good agreement with the experimental spectrum. Therefore,

https://doi.org/10.1017/S0885715619000617 Published online by Cambridge University Press

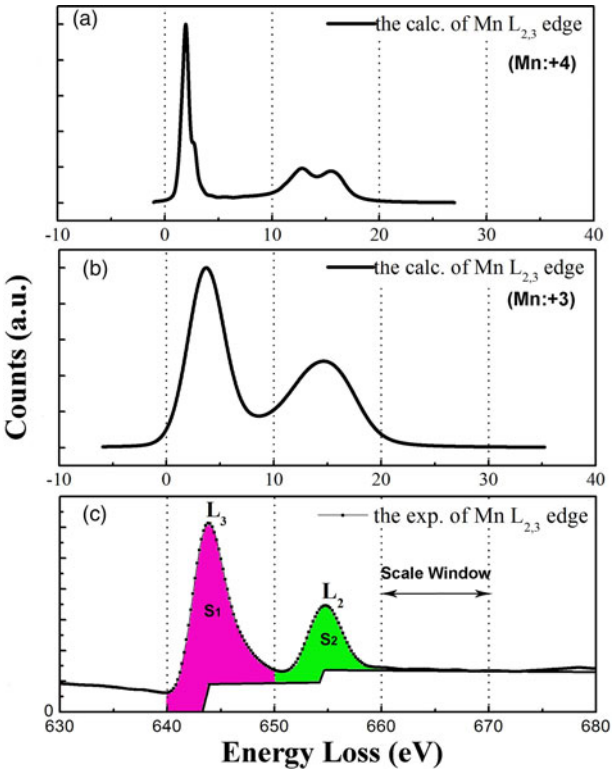

Figure 6. (a) The simulation spectrum of Mn $L_{2,3}$ edge in Mn (+4). (b) The simulation spectrum of Mn $L_{2,3}$ edge in Mn (+3). (c) The experimental spectrum used to estimate the ratio of L_3/L_2. To extract the L_3 and L_2 peak intensities for the Mn L_3/L_2 ratio, a Hartree–Slater cross-section function was used as a step function scaled to the 10 eV wide region immediately to the right of the L_2 peak. Then, the energy ranges of 10.0 eV of L_3 and L_2 peaks were integrated.

we confirmed that the element of Mn is trivalent oxidation state in $YMnO_3$.

IV. CONCLUSIONS

In summary, the electronic structure of $YMnO_3$ was investigated systematically based on both EELS and first-principle calculations. The XRD and SAED experiments revealed that the sample was pure hexagonal $YMnO_3$ and the Mn is bipyramidal coordinated. Assignments of the individual interband transitions have been accomplished by comparing the interband transition energy with the calculated PDOS. The analysis from the DOS, low energy loss spectrum, and high-energy loss spectrum of the O K-edge, the ferroelectricity of $YMnO_3$ is related to the hybridization (O 2p and Mn 3d, O 2p and Y 4d, respectively) and the forming of covalent bonds. In addition, the experimental spectrum of O K-edge is in good agreement with the simulated spectrum. The fine structure of Mn $L_{2,3}$ edge confirmed that Mn ion in the $YMnO_3$ belongs to trivalent oxidation state.

Acknowledgement We appreciate the useful suggestions from Xiaofeng Duan and Xing Lu. We also acknowledge the help of Zhiqiang Li during the cause of experiments.

FUNDING

This work was sponsored by National Natural Science Foundation of China under Grant Nos. 51672057, 51722205 and 51872034. This work was sponsored by Liaoning revitalization talents program under No. XLYC1807173 and the outstanding talents support the program by Dalian city under No. 2015R004. This work was also sponsored by Key Projects of Natural Science Foundation of Liaoning and Doctor Start-up Fund of Liaoning under Grant No. 20170520155.

Babu, J. B., He, M., and Zhang, D. F. (**2007**). "Enhancement of ferroelectric properties of $Na_{1/2}Bi_{1/2}TiO_3$-$BaTiO_3$ single crystals by Ce dopings," Appl. Phys. Lett. **90**, 102901.

Bi, K., Wang, X. Y., Hao, Y. N., Lei, M., Dong, G. Y., and Zhou, J. (**2019**). "Wideband slot-coupled dielectric resonator-based filter," J. Alloys Compd. **785**, 1264–1269.

Cho, D. Y., Kim, J. Y., Park, B. G., Rho, K. J., Park, J. H., Noh, H. J., and Kim, B. J. (**2007**). "Ferroelectricity driven by Y d^0-ness with rehybridization in $YMnO_3$," Phys. Rev. Lett. **98**, 217601.

Cohen, R. E. (**1992**). "Origin of ferroelectricity in perovskite oxides," Nature. **358**, 136–138.

Du, Y. X., Lei, M., Chen, X. L., and Zhang, D. F. (**2008**). "Influence of 90° domain switching on the physical properties of tetragonal barium titanate single crystals," Physica B. **403**, 3018–3021.

Egerton, R. F. (**2009**). "Electron energy-loss spectroscopy in the TEM," Rep. Prog. Phys. **72**, 16502.

Egerton, R. F., Crozier, P. A., and Rice, P. (**1987**). "Electron energy-loss spectroscopy and chemical change," Ultramicroscopy. **23**, 305–312.

Erni, R., and Browning, N. D. (**2005**). "Valence electron energy-loss spectroscopy in monochromated scanning transmission electron microscopy," Ultramicroscopy. **104**, 176–192.

Filippetti, A., and Hill, N. A. (**2002**). "Coexistence of magnetism and ferroelectricity in perovskites," Phys. Rev. B. **65**, 195120.

Ghosez, P., Michenaud, J.-P., and Gonze, X. (**1998**). "Dynamical atomic charges: The case of ABO_3compounds," Phys. Rev. B. **58**, 6224.

Gibbs, A. S., Knight, K. S., and Lightfoot, P. (**2011**). "High-temperature phase transitions of hexagonal $YMnO_3$," Phys. Rev. B. **83**, 955.

He, X., Luan, S. Z., Wang, L., Wang, R. Y., Du, P., Xu, Y. Y., Yang, H. J., Wang, Y. G., Huang, K., and Lei, M. (**2019**). "Facile loading mesoporous Co_3O_4 on nitrogen doped carbon matrix as an enhanced oxygen electrode catalyst," Mater. Lett. **244**, 78–82.

Huang, Z. J., Cao, Y., Sun, Y. Y., Xue, Y. Y., and Chu, C. W. (**1997**). "Coupling between the ferroelectric and antiferromagnetic orders in $YMnO_3$," Phys. Rev. B. **56**, 2623.

Ikeno, H., and Mizoguchi, T. (**2017**). "Basics and applications of ELNES calculations," Microscopy. **66**, 305–327.

Kim, Y. J., Bhatnagar, A., Pippel, E., Alexe, M., and Hesse, D. (**2014**). "Microstructure of highly strained $BiFeO_3$ thin films: transmission electron microscopy and electron-energy loss spectroscopy studies," J. Appl. Phys. **115**, 043526.

Kimura, T., Goto, T., Shintani, H., Ishizaka, K., Arima, T., and Tokura, Y. (**2003**). "Magnetic control of ferroelectric polarization," Nature. **426**, 55–58.

Lima, A. F., and Lalic, M. V. (**2013**). "Analysis of orbital hybridization in the magnetoelectric YMnO3 crystal from first principles calculations," IEEE Trans. Magn. **49**, 4687–4690.

Lin, S., Bai, X. P., Wang, H. Y., Wang, H. L., Song, J. N., Huang, K., Wang, C., Wang, N., Li, B., Lei, M., and Wu, H. (**2017**). "Roll-to-roll production of transparent silver nanofiber network electrode for flexible electrochromic smart windows," Adv. Mater. **29**, 1703238.

Lin, S., Wang, H. Y., Zhang, X. N., Wang, D., Zu, D., Song, J. N., Liu, Z. L., Huang, Y., Huang, K., Tao, N., Li, Z. W., Bai, X. P., Li, B., Lei, M., Yu, Z. F., and Wu, H. (**2019a**). "Direct spray-coating of highly robust and transparent Ag nanowires for energy saving windows," Nano Energy. **62**, 111–116.

Lin, S., Wang, H. Y., Wu, F., Wang, Q. M., Bai, X. P., Zu, D., Song, J. N., Wang, D., Liu, Z. L., Li, Z. W., Tao, N., Huang, K., Lei, M., Li, B., and Wu, H. (**2019b**). "Room-temperature production of silver-nanofiber film for large-area, transparent and flexible surface electromagnetic interference shielding," Flexible Electron. **3**, 6.

Liu, S. H., Huang, J. C. A., and Qi, X. D. (**2011**). "Structural transformation and charge transfer induced ferroelectricity and magnetism in annealed $YMnO_3$," AIP Adv. **1**, 032173.

Malo, S., and Maignan, A. (**2012**). "Co-substitution at the Mn-site in $YMnO_3$: structural stability and physical properties," Mater. Res. Bull. **47**, 974–979.

Nishida, S. J., Kobayashi, S. S., Kumamoto, A., Ikeno, H., Mizoguchi, T., Tanaka, I., Ikuhara, Y. C., and Yamamoto, T. (**2013**). "Effect of local coordination of Mn on Mn–$L_{2,3}$ edge electron energy loss spectrum," J. Appl. Phys. **114**, 054906.

Perdew, J. P., Burke, K., and Ernzerhof, M. (**1996**). "Generalized gradient approximation made simple," Phys. Rev. Lett. **77**, 3865–3868.

Prikockyte, A., Bilc, D., Hermet, P., Dubourdieu, C., and Ghosez, P. (**2011**). "First-principle calculations of the structural and dynamical properties of ferroelectric $YMnO_3$," Phys. Rev. B. **84**, 214301.

Quhe, R. G., Liu, J. C., Wu, J. X., Yang, J., Wang, Y. Y., Li, Q. H., Li, T. R., Yang, J. B., Peng, H. L., Lei, M., and Lu, J. (**2019**). "High-performance Sub-10 nm monolayer Bi_2O_2Se transistors," Nanoscale. **11**, 532–540.

Rafferty, B., Pennycook, S., and Brown, L. M. (**2000**). "Zero loss peak deconvolution for bandgap EEL spectra," J. Electron. Microsc. **49**, 517–524.

Salazar-Kuri, U., Mendoza, M. E., and Siqueiros, J. M. (**2012**). "Phase transition in multiferroic $YMnO_3$ and its solid solution $YMn_{(0.93)}Fe_{(0.07)}O_3$," Physica B. **407**, 3551–3554.

Schmid, H. K., and Mader, W. (**2006**). "Oxidation states of Mn and Fe in various compound oxide systems," Micron. **37**, 426–432.

Sotero, W., Lima, A. F., and Lalic, M. V. (**2015**). "Analysis of the Mn–O and Y–O bonds in paraelectric and ferroelectric phase of magnetoelectric $YMnO_3$ from the first principles calculations," J. Alloys Compd. **649**, 285–290.

Varela, M., Oxley, M. P., Luo, W., Tao, J., Watanabe, M., Lupini, A. R., Pantelides, S. T., and Pennycook, S. J. (**2009**). "Atomic-resolution imaging of oxidation states in manganites," Phys. Rev. B. **79**, 085117.

Wang, H., Liu, R. P., Li, Y. T., Lu, X. J., Wang, Q., Zhao, S. Q., Yuan, K. J., Cui, Z. M., Li, X., Xin, S., Zhang, R., Lei, M., and Lin, Z. Q. (**2018**). "Durable and efficient hollow porous oxide spinel microspheres for oxygen reduction," Joule. **2**, 337–348.

Wang, S., Xu, H. D., Cai, J., Wang, Y. P., Tao, H. L., Cui, Y., He, M., Song, B., and Zhang, Z. H. (**2019a**). "Electronic structure of multiferroic $BiFeO_3$: electron energy-loss spectroscopy and first-principles study," Micron. **120**, 43–47.

Wang, X. T., Cui, Y., Li, T., Lei, M., Li, J. B., and Wei, Z. M. (**2019b**). "Recent advances in the functional 2D photonic and optoelectronic devices," Adv. Opt. Mater. **7**, 1801274.

Zhang, Z. H., Qi, X. Y., Jian, J. K., and Duan, X. F. (**2006**). "Investigation on optical properties of ZnO nanowires by electron energy-loss spectroscopy," Micron. **37**, 229–233.

Zhang, Z. H., Yang, J. J., He, M., Wang, X. F., and Li, Q. (**2008**). "Electronic structure of a potential optical crystal $YBa_3B_9O_{18}$: experiment and theory," Appl. Phys. Lett. **92**, 171903.

Zhang, Q. H., Guo, S. D., Ge, B. H., Chen, P., Yao, Y., Wang, L. J., and Gu, L. (**2014**). "A new ferroelectric phase of $YMnO_3$ induced by oxygen-vacancy ordering," J. Am. Ceram. Soc. **97**, 1264–1268.

https://doi.org/10.1017/S0885715619000617 Published online by Cambridge University Press